Role of deformations and orientation effects in binary and ternary decay of the ^{252}Cf nucleus

Chahat Jindal and Manoj K. Sharma*
Department of Physics and Material Science, Thapar Institute of Engineering and Technology, Patiala 147004, India

(Received 10 January 2024; revised 28 February 2024; accepted 15 April 2024; published 7 May 2024)

The phenomenon of spontaneous fission, which includes both binary and ternary decay modes, is observed within heavy and superheavy nuclei. Extensive efforts have been made to investigate the binary and ternary decay patterns exhibited by various nuclei belonging to the heavy-mass region. In this context, our study systematically examines the ground-state binary and ternary decay mechanisms of the ^{252}Cf nucleus. To accomplish this, we have used the quantum mechanical fragmentation theory approach. It is known that the orientation angles of the decaying fragments play an important role in mass distribution. Therefore, in the present work probable orientation (both optimum and fixed) effects with deformations (up to quadrupole β_2) of nuclei participating in the fragmentation process are taken into account. Further, the fission fragments for binary ($A_1 + A_2$) and for ternary ($A_1 + A_2 + A_3$) decay processes are identified by selecting channels of local minima in the fragmentation potential, with the third fragment A_3 being ^{4}He for the ternary fission. The inclusion of hot-compact/$(90^\circ-90^\circ)$/$(0^\circ-90^\circ)$/$(90^\circ-0^\circ)$ orientations leads to the emergence of symmetric fission fragments, where shell effects are found to play the key role, whereas the cold-elongated/$(0^\circ-0^\circ)$ leads to the participation of highly deformed nuclei with large mass asymmetry. In addition to this, two types of tripartition of the radioactive nucleus are considered: equatorial cluster tripartition and collinear cluster tripartition. Both configurations are studied by considering $A_3 = {}^{30}$Mg and ^{48}Ca as fixed fragments. The most probable fragments in the exit channel [^{72}Ni($Z = \mathbf{28}$, $N = 44$) + ^{132}Sn($Z = \mathbf{50}$, $N = \mathbf{82}$)+ ^{48}Ca($Z = \mathbf{20}$, $N = \mathbf{28}$)] indicate that the deformations and the proton/neutron shell closure play a vital role in the spontaneous fission analysis of binary and ternary channels. The calculated results are aligned with available experimental data. In addition to this, relative yield for different ternary combinations is calculated for the ^{252}Cf nucleus.

DOI: 10.1103/PhysRevC.109.054607

I. INTRODUCTION

The first [1–4] direct observation of spontaneous binary fission of ^{252}Cf was achieved by using multiple Ge detectors and implementing gammasphere. Besides binary fission, ternary fission of ^{252}Cf [5–11] was also observed as a probable spontaneous fission mode. Muga *et al.* [12] used the nuclear emulsion technique to photograph the three fragments emitted in spontaneous ternary fission of ^{252}Cf. A large variety of light-charged ternary particles like ^{3,2,1}H, ^{8,6,5,4,3}He, ^{8}Li, ^{10}Be, and ^{14}C have been observed by various authors [2,13–20]. Goodin *et al.* [21] conducted a comprehensive investigation into the bimodal fission of ^{252}Cf. Their study observed various binary channels, including Xe-Ru and Ba-Mo, alongside ternary channels such as Ba-α-Zr, Mo-α-Xe, and Te-α-Ru. Ramayya *et al.* [20,22] identified different fragment channels in the cold spontaneous fission of binary (Zr+Ce, Mo+Ba, Tc+Cs, Ru+Xe, Pd+Te) and ternary (Kr+Nd+He, Sr+Ce+He, Zr+Ba+He, Mo+Xe+He, Ru+Te+He, Pd+Sn+He) decay of ^{252}Cf. Aside from light ternary particles, there is also the possibility of emission of heavy third fragments like C, N, O, F, Ne, Na, Mg, Al, and Si reported in Refs. [23–31]. Moreover, the prospect of true ternary fission (TTF), characterized by the radioactive nucleus fragmenting into three entities of comparable masses was reported in Refs. [32,33]. It should be noted here that spontaneous TTF has not been experimentally observed but some experimental signature of induced TTF exists, where heavier third fragments were identified [23–26]. It was observed that fission fragments and potential energy surfaces depend on the mass distribution of the fissioning nucleus. In view of this, we intend to explore the binary and ternary fragments of ^{252}Cf, for further clarity of the decay dynamics of heavy nuclei.

Many experimental and theoretical [14,34–39] studies show that the most observed light ternary particle is the α particle. The angular distribution analysis of light-charged-ternary particles indicates their formation in the neck region of two primary fission fragments. Consequently, these particles are emitted in a direction perpendicular to the fission axis. The process in which the emission of a third particle occurs in the direction perpendicular to the fission axis is known as equatorial cluster tripartition (ECT). On the other hand, if the emitted third fragment is in the direction of the fission axis, then it is called collinear cluster tripartition (CCT) [40]. Recently, an extensive search of ternary fragments was performed using the missing mass approach with two FOBOS detectors for spontaneous fission of ^{252}Cf and thermal neutron-induced fission of ^{235}U(n_{th},f) [41–44]. The FOBOS setup detected fragments

*jindalchahat11@gmail.com

 ©2024 American Physical Society

like Ni/Sn, while the determination of the third fragment was accomplished using the missing mass technique. As a result, three fragments with proton magic numbers $Z = 50$, 28, and 20 were observed, each possessing comparable masses. Earlier studies show that the ECT is suited for light-charged-accompanied fission while CCT is more suitable heavy-third fragment [15,33,45–48]. It may be noted that the deformations [49–54] play a crucial role in the binary fragmentation for the appropriate prediction of the favorable fragments and their respective yields [55]. Gupta *et al.* [56,57] calculated the fragmentation potential in view of the collision of two deformed and oriented nuclei, including deformations for coplanar and non-co-planar cases. Also, they have calculated the role of deformations and compact orientation in fusion-fission reaction [58]. Recently, excitation-energy-dependent potential energy surfaces for tripartition of ^{252}Cf were studied by taking orientation angles as $0^\circ-0^\circ$ [59]. Many authors [35,37,60–64] investigated the importance of deformations and orientations in binary and ternary fission of various nuclei in the ground and excited states. This work is devoted to analyzing both decay modes simultaneously (binary and ternary) for ^{252}Cf nucleus by including the deformation and orientation effect.

Based on the preceding discussion, the primary objective of this paper is to achieve the following goals within the framework of quantum mechanical fragmentation theory (QMFT): (i) investigate the influence of deformations and orientations for binary and ternary channels, (ii) identify the most likely fission fragments for both binary and ternary decay scenarios, and (iii) compare the ECT and CCT modes by considering the lighter and heavier fixed third fragments.

The outline of this paper is as follows: In Sec. II, the methodology is explored. The collective clusterization-based preformed cluster model (PCM) and the three cluster model (TCM) is employed to examine the processes of binary and ternary decay. Section III delves into the exploration of the behavior of binary and ternary fragmentation potentials, taking into account the incorporation of deformation and orientation effects. Also, the relative yield of different ternary combinations is studied in this section. Last, Sec. IV presents a summary of the observed outcomes.

II. THEORETICAL FRAMEWORK

The binary and ternary fission analysis is carried out using the PCM and TCM within the framework of QMFT [65]. QMFT is a unified description to understand decay dynamics and is worked out in mass and charge asymmetry coordinate represented as $\eta_A = \frac{(A_1-A_2)}{(A_1+A_2)}$ and $\eta_z = \frac{(Z_1-Z_2)}{(Z_1+Z_2)}$. Here subscripts 1 and 2 denote the light and heavy fragments. For ternary fission, the third fragment is considered fixed, and these asymmetry coordinates are applicable for light and heavier fragments only. Apart from these coordinates, relative separation distance (R) between colliding nuclei, multipole deformations ($\beta_{\lambda i}$) of colliding nuclei, azimuthal angle ϕ between the principal planes of two deformed fragments, neck parameter ϵ are another four coordinates used to define the nuclear shape. Further, a brief description of PCM and TCM is given in the following subsections.

1. Preformed cluster model

PCM [66–68] is based on the assumption that the decaying fragments are preformed as separate entities inside the parent nucleus before the actual decay process takes place. In PCM, the most probable fragments can be identified in terms of the fragmentation potential and preformation probability. The two body fragmentation potential is given as [69]:

$$V_R(\eta, R) = \sum_{i=1}^{2} B(A_i, Z_i) + V_P(A_i, R, \beta_{\lambda i}, \theta_i, \phi) + V_C(Z_i, R, \beta_{\lambda i}, \theta_i, \phi). \quad (1)$$

Here $B(A_i, Z_i)$ (taken from Refs. [70,71]) denotes the binding energy of the fragment i and V_P and V_C are respectively the nuclear proximity and Coulomb potential. For more details see Refs. [72]. Here deformation (β_2) and orientation (θ_i) effects are included through nuclear and Coulomb potentials (explained later).

2. Three cluster model

TCM [14,15,35,37,73] is an extension of PCM, specifically focusing on the three-body decay dynamics. In TCM, the decay process involves the emission of three fragments (clusters) from the parent nucleus. It is studied in terms of coordinates η (mass-asymmetry parameter) and R (internuclear distance). In ternary fission, three fragments are emitted with $A_1 \geqslant A_2 \geqslant A_3$. Until now, most of the work done by TCM is done by taking the spherical choice of decaying fragments [15,73]. In the present work, deformation effects are incorporated in fragments A_1 and A_2, where the third fragment (A_3) is considered spherical. Deformations up to quadrupole (β_2) are included with consideration of optimum as well as specific-fixed orientations. For optimum orientations, θ_i are taken from Table I of Ref. [57], i.e., hot-compact and cold-elongated configurations. The angles are uniquely fixed on the basis of signs of their corresponding quadrupole deformations [57]. The optimum orientations are of two types, i.e., hot-compact (also referred to as the belly-to-belly configuration) and cold-elongated (also known as pole-to-pole configuration). In fixed orientations, the values of θ are predetermined [$(90^\circ, 90^\circ)$, $(0^\circ-0^\circ)$, $(0^\circ-90^\circ)$, and $(90^\circ-0^\circ)$], independent of the choice of deformation signs. Figures 1(a)–1(d) correspond to $(90^\circ, 90^\circ)$, $(0^\circ, 0^\circ)$, $(0^\circ, 90^\circ)$, and $(90^\circ, 0^\circ)$, respectively. Specifically where both β_{21} and β_{22} are $\geqslant 0$, whereas, when both β_{21} and β_{22} $\leqslant 0$, then these configurations transform to $(0^\circ, 0^\circ)$, $(90^\circ, 90^\circ)$, $(0^\circ, 90^\circ)$, and $(90^\circ, 0^\circ)$, respectively. Similarly for β_{21} $\geqslant 0$ and β_{22} $\leqslant 0$ these configurations transformed into $(90^\circ, 0^\circ)$, $(0^\circ, 90^\circ)$, $(90^\circ, 90^\circ)$, and $(0^\circ, 0^\circ)$ and vice versa for β_{21} $\leqslant 0$ and β_{22} $\geqslant 0$. In this context, θ_i represents the angular deviation between the collision axis and the symmetry axis. Meanwhile, α_i signifies the deviation between the symmetry axis and the radius vector of the nuclei. Notably, θ_i is measured in a clockwise direction from the nuclear symmetry axis, whereas the rotational orientation α_i of each nucleus is measured in the counterclockwise direction from the collision z axis. As a first step, we can calculate the fragmentation

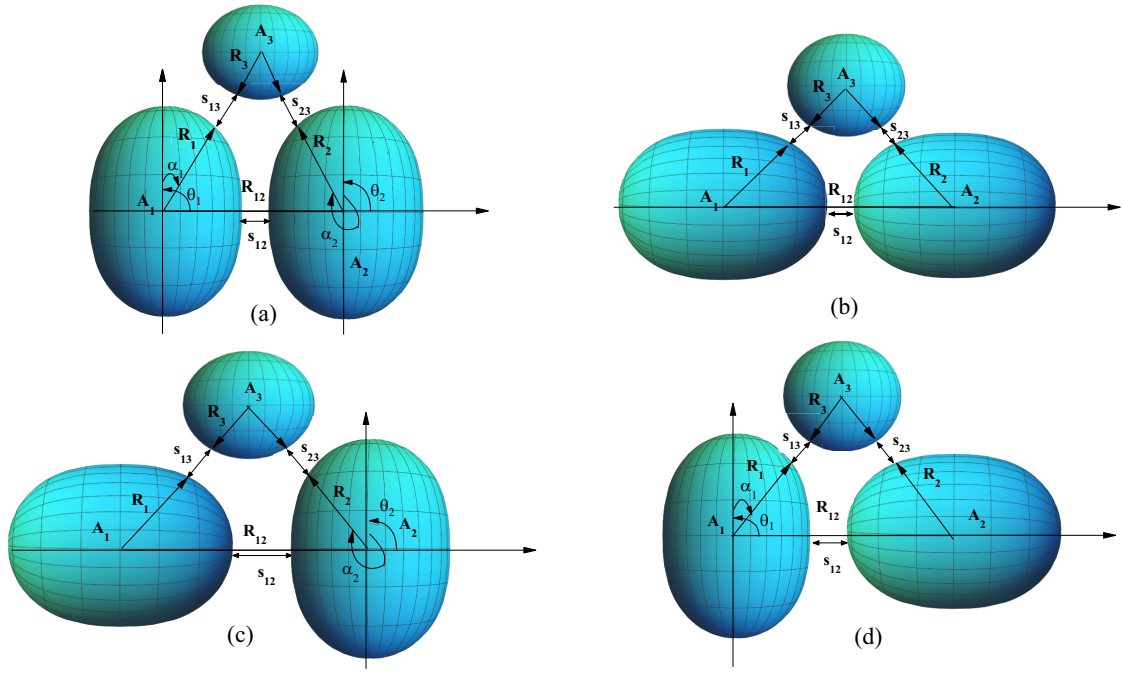

FIG. 1. Schematic diagram of an equatorial configuration of two deformed heavy nuclei (A_1 and A_2) with the spherical third fragment ($A_3 = {}^4$He) $(\theta_1, \theta_2) =$ (a) 90°−90°, (b) 0°−0°, (c) 0°−90°, and (d) 90°−0° with $\beta_{21}, \beta_{22} \geqslant 0$.

potential for the tripartition process and can be written as:

$$V_R(\eta, R) = \sum_{i=1}^{3}\sum_{j>i}^{3} B_i(A_i, Z_i) + V_{Cij}(R, Z_i, \beta_{\lambda i}, \theta_i, \phi) + V_{Pij}(R, A_i, \beta_{\lambda i}, \theta_i, \phi), \quad (2)$$

where B_i are the binding energies of the fragments, taken from Refs. [70,71]. The potential V_{Cij} and V_{Pij} are Coulomb and proximity potential can be written as [35,57,74]:

$$V_{Cij}(Z_i, \beta_{\lambda i}, \theta_i, \alpha_i) = \frac{Z_i Z_j e^2}{R} + 3Z_i Z_j e^2 \sum_{\lambda, i=1,2} \frac{1}{2\lambda+1} \times \frac{R_i^{\lambda}(\alpha_i)}{R^{\lambda+1}} Y_{\lambda}^{(0)}(\theta_i)\left[\beta_{\lambda i} + \frac{4}{7}\beta_{\lambda i}^2 Y_{\lambda}^{(0)}(\theta_i)\right] \quad (3)$$

$$V_{Nij}(\xi) = 4\pi \overline{R}\gamma b \Phi(s). \quad (4)$$

In Eq. (3), Z_i and Z_j are the charge numbers and $e^2 = 1.44$ MeV fm. The relative separation between any two participating nuclei i and j ($i, j = 1, 2, 3$) is as follows:

$$R_{ij} = R_i + R_j + s_{ij}, \quad (5)$$

where R_i represents the radius vector of fragments also shown in Fig. 1 and can be represented as:

$$R_i(\alpha_i) = R_{0i}\left[1 + \sum_{\lambda} \beta_{\lambda i} Y_{\lambda}^{(0)}(\alpha_i)\right], \quad (6)$$

where R_{0i} is

$$R_{0i} = \left[1.28A_i^{\frac{1}{3}} - 0.76 + 0.8A_i\right] \text{fm}. \quad (7)$$

In this context "s_{ij}" represents the relative separation between the fragments as shown in Fig. 1. The value of this parameter is influenced by the arrangement of three specific fragments, namely ECT and CCT discussed later in Fig. 4. In ECT, the surface separation distance between each fragment can be expressed by [15,36]:

$$s_{12} = s_{23} = s_{31} = s, \quad (8)$$

whereas for CCT the surface separation is [36]

$$s_{12} = 2(R_3 + s), s_{23} = s_{31} = s. \quad (9)$$

In Eq. (4), the universal function $\Phi(s)$ depends only on the distance between two nuclei and is independent of the atomic numbers of the two nuclei and is given as [75]:

$$\phi(\xi) = \begin{cases} -1/2(\xi - 2.54)^2 - 0.0852(\xi - 2.54)^3 & \xi < 1.2511 \\ -3.437\exp[\frac{-\xi}{0.75}] & \xi \geqslant 1.2511, \end{cases} \quad (10)$$

where $\xi = s/b$ and b is the diffuseness of the nuclear surface ($b = 1$ fm). The factor γ is the nuclear energy coefficient is given by $\gamma = 0.9517[1 - 1.7826[(N - Z)/A]^2]$ MeV fm^{-2} and $\overline{R}$ is the mean curvature radius defined for the deformed reaction partners as:

$$\frac{1}{\overline{R}^2} = \frac{1}{R_{11}R_{12}} + \frac{1}{R_{21}R_{22}} + \frac{1}{R_{11}R_{22}} + \frac{1}{R_{21}R_{12}}. \quad (11)$$

The principal radii of curvature R_{11}, R_{12}, R_{21}, and R_{22} are given by Balts and Bayman [76]. Then the penetration

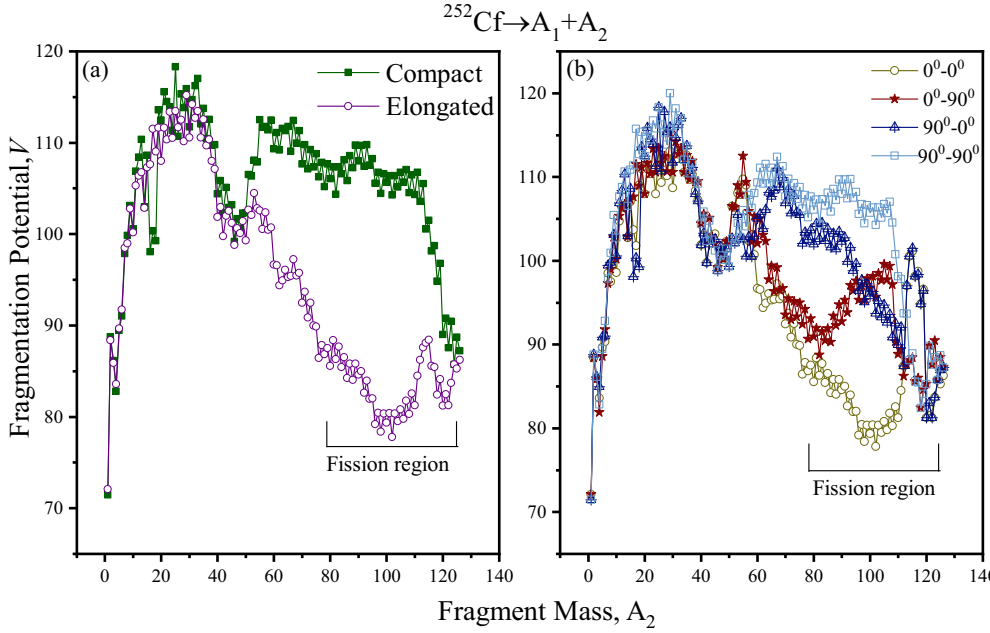

FIG. 2. Binary fragmentation potential V (MeV) is plotted with respect to fragment mass number A_2 for ^{252}Cf calculated with inclusion of quadrupole deformation (β_2) (a) with optimum orientation (hot-compact and cold elongated) (b) with fixed orientation [where $(\theta_1, \theta_2) = (90^\circ{-}90^\circ)$, $(0^\circ{-}0^\circ)$, $(0^\circ{-}90^\circ)$, and $(90^\circ{-}0^\circ)$].

probability of three-body decay channel is estimated as

$$P = \exp\left[-\frac{2}{\hbar}\int_{s_1}^{s_2}\{2\mu[V(R)-Q]\}^{1/2}ds\right]. \quad (12)$$

Here s_1 and s_2 are the first and second turning points satisfying the $V(s_2) = Q(Q$ value). μ is the reduced mass of the three fragments,

$$\mu_{123} = \left(\frac{\mu_{12}A_3}{\mu_{12}+A_3}\right)m, \quad (13)$$

where $\mu_{12} = A_1A_2/(A_1+A_2)$ and m is the nucleon mass. The relative yields for the fragmentation channels of the ternary processes are calculated as the ratio between the penetration probability of a given fragment pair over the sum of penetration probabilities of all possible fragments as

$$Y(A_i, Z_i) = \frac{P(A_i, Z_i)}{\Sigma P(A_i, Z_i)}. \quad (14)$$

III. DISCUSSION

This section provides the theoretical overview of the binary and ternary decay of ^{252}Cf nucleus. Section III A analyzes the binary and ternary fragmentation behavior using deformations (up to β_2-quadrupole deformations) and corresponding orientations (optimum and fixed). The decay fragments are identified and compared with available experimental and theoretical observations. Section III B presents a comparison between ECT and CCT, configurations by taking third fragments as ^{30}Mg and ^{48}Ca using TCM. Further, Sec. III C presents the relative yield for spontaneous decay of ^{252}Cf by considering different A_3 combinations, i.e., ^{4}He, ^{30}Mg, and ^{48}Ca.

A. Binary and ternary decay of ^{252}Cf

In a nuclear reaction experiment, the positioning and choice of the detector can be determined by various factors like angles, energies involved in the reaction, and symmetry or asymmetry of the reaction products. Therefore, in the present work, an effort is made to encompass the diverse angles of the decaying fragments. An effort is made to understand how orientation angles change mass distribution of the decaying fragments. In order to comprehend the nuclear dynamics of a radioactive nucleus, we undertake the calculations of the collective potential energy, also known as the fragmentation potential [as depicted in Eqs. (1) and (2) for binary and ternary decay, respectively]. These results investigate the relative stability of decaying fragments by examining the profound valley within the fragmentation potential across all η values. This study incorporates deformation effects up to quadrupole (β_2) deformations, both with and without optimum orientation. Optimum orientation is obtained on the basis of prolate and oblate shapes of β_2 deformations. For optimum orientation, angles are uniquely fixed, which result in "hot-compact" and "cold-elongated" configurations (for a comprehensive explanation of optimal orientation [57]). In the present work, we denote hot-compact as compact and cold-elongated as elongated orientations. Furthermore, fixed orientations are characterized by specific values of θ_1, θ_2 [$(\theta_1, \theta_2 = (0^\circ{-}0^\circ)$, $(0^\circ{-}90^\circ)$, $(90^\circ{-}0^\circ)$, and $(90^\circ{-}90^\circ)$], independent of the shape of nuclei as explained earlier in Fig. 2.

The binary fragmentation potential $V_R(\eta)$ (or V) is calculated using Eq. (1) and plotted with respect to fragment mass A_2. Here the values for quadrupole deformations are sourced from Ref. [71]. It is noteworthy to mention here

that, during calculations, we observe a distinctive dip in the asymmetric fragmentation combinations such as $^{17}B + ^{235}Np$, $^{18}C + ^{234}U$, $^{54}K + ^{198}Au$, and $^{55}K + ^{197}Au$. These dips are attributed to exceedingly negative deformation values in one of the decaying fragments [^{17}B (−0.398), ^{18}C (−0.353), ^{54}K (−0.373), and ^{55}K (−0.398)]. However, due to their correspondingly minute penetrability values, these dips have minimal impact on the overall fragmentation potential [77]. To rectify these dips within the fragmentation potential, the deformation parameters for these fragments (^{17}B, ^{18}C, ^{54}K, ^{55}K) are taken from the RMF model [78–80]. Further, using new deformation values for the above-mentioned nuclei, fragmentation potential is plotted with respect to A_2 in Fig. 2. The fragmentation potential depicted in Fig. 2(a) has been computed for both hot-compact (compact) and cold-elongated (elongated) configurations. In Fig. 2(b) the fragmentation potential is compared by taking fixed orientations where specific values of θ_1 and θ_2 are taken [$(\theta_1, \theta_2) = (90°-90°)$, $(0°-0°)$, $(0°-90°)$, and $(90°-0°)$]. It shows that different orientations significantly affect the structure and magnitude of the fragmentation potential. The cold-elongated orientation (also called as pole-to-pole configuration [57]) yield lower magnitude of fragmentation potential as the interaction radius is the largest. At this (pole-to-pole) orientation, the symmetry axis of both the deformed fragments lies along a straight line, whereas hot-compact configuration (also called as belly-to-belly configuration) gives the highest potential as the interaction radius is lowest. A thorough examination of Fig. 2(a) shows that symmetric fission is prominent for compact configuration, whereas the dominance of asymmetric fission fragments is seen for elongated configuration. However, for fixed orientations, the symmetric as well as asymmetric fission fragments are observed. The configuration with angles $0°-0°$ results in the formation of asymmetric fragments, whereas configurations with angles $0°-90°$, $90°-90°$, and $90°-0°$ tend to give nearly symmetric fragments. This is due to the fact that most of the nuclei in the region ($100 \leqslant A_2 \leqslant 110$) are of prolate deformed nuclei (as shown in Table I), which with angle $0°-0°$ will give a configuration where the interaction radius is maximum and hence potential energy (fragmentation potential) is minimum. On the other hand, the $90°-90°$ configuration corresponds to the configuration with the smallest interaction radius, resulting in the highest potential energy. In contrast, the $0°-90°$ and $90°-0°$ configurations fall in between, with intermediate interaction radii and, consequently, intermediate potential energy levels. However, A_2 ranging from 116 to 126, the nuclei typically exhibit either oblate or spherical shapes. In this case, the $0°-0°$ orientation minimizes the radius, resulting in an increase in potential energy, while the opposite holds true for the $90°-90°$ configuration.

It is clear from the above analysis that the deformation and orientation significantly influence the fragment mass distribution as the fragmentation potential and barrier height depend on the choice of the radius vector. The specific fission fragments identified within this region are detailed in the first and third columns of Table I. Below all the fragments the combination of (N_1, Z_1+ N_2, Z_2) with corresponding deformations values are mentioned in Table I. As we have done minimization with mass number the mass fragments from $100 \leqslant A_2 \leqslant 116$ are identified. This shows a reasonable agreement with experimental data [20,22]. From all the identified fission fragments the fragments like ^{100}Zr ($N_1 = 60$, $Z_1 = 40$) + ^{152}Ce, ^{102}Zr ($N_1 = 62$, $Z_1 = 40$) + ^{150}Ce, ^{103}Zr ($N_1 = 63$, $Z_1 = 40$) + ^{149}Ce, ^{104}Zr ($N_1 = 64$, $Z_1 = 40$) + ^{148}Ce, ^{106}Mo ($N_1 = 64$, $Z_1 = 42$) + ^{146}Ba, ^{107}Mo ($N_1 = 65$, $Z_1 = 42$) + ^{145}Ba, ^{108}Mo ($N_1 = 66$, $Z_1 = 42$) + ^{144}Ba, ^{114}Ru ($N_1 = 70$, $Z_1 = 44$) + ^{138}Xe, and $^{116}Pd + ^{136}Te$ ($N_1 = 84$, $Z_1 = 52$) were experimentally observed [20,22]. Notably, the spherical magic shell closure ($Z = 50$, $N = 82$) significantly determines the favored fragment in the context of the hot-compact/$(90°-90°, 0°-90°, 90°-0°)$ configuration. Conversely, the deformed magic shell closures ($Z = 38$, $N = 60$, and 62) and deformations play pivotal roles in instances of cold-elongated/$(0°-0°)$ configurations. Consequently, it can be ascertained that both spherical and deformed shell closures, alongside deformations up to quadrupole, are important for identifying the fragments of exit channel. Further, the possibility of ternary decay of the ^{252}Cf nucleus is investigated within TCM [35]. The ternary fragmentation potential using Eq. (2) is calculated for the considered radioactive nucleus using the assumption of equatorial configuration [14,15,73] with fixed spherical third fragment ($A_3 = {}^4He$) and plotted in Fig. 3 as a function of A_2. The calculations are made at surface separation $s = 1.0$ fm. This choice of surface separation (s) is taken from Refs. [15,73]. The three-body fragmentation potential is calculated by taking ^4He accompanied by ternary fission of ^{252}Cf. This calculation is conducted both with and without optimum orientations, as explained earlier. The resulting potentials are depicted in Fig. 3, illustrating the relationship between fragment mass number A_2 and the potential energy. Figure 3(a) showcases the fragmentation potential between three fragments for both compact and elongated orientations. Similarly, in Fig. 3(b), the fragmentation potential calculated for certain fixed orientation. It shows that cold-elongated configuration gives lower potential as it corresponds to the maximum interaction radius [57], whereas the potential is relatively high for compact configuration due to the minimum radius. Evidently, altering the orientation significantly modifies the distribution of fission fragment masses. This phenomenon is rooted in the diminishing influence of spherical shell effects with the incorporation of elongated orientations and the increasing influence of deformed shell closure. This interplay leads to symmetric mass distributions for the compact orientation and asymmetric distributions for the elongated orientation. However, for fixed orientations (where θ_1 and θ_1 are set some specific values), asymmetric and symmetric mass distributions can be seen. Notably, it should be emphasized that nuclei within the fission region ($92 \leqslant A_2 \leqslant 110$) are predominantly prolate-deformed nuclei, which potentially influence the fragmentation potential. Further, the minimized fission fragments for different sets of orientations are given in the second and fourth columns of Table I. Of the identified fragments, the fragments ^{92}Kr($N_1 = 56$, $Z_1 = 36$)+ ^{156}Nd, ^{96}Sr($N_1 = 58$, $Z_1 = 38$)+ ^{152}Ce, ^{98}Sr($N_1 = 60$, $Z_1 = 38$)+ ^{150}Ce, ^{99}Sr ($N_1 = 61$, $Z_1 = 38$)+ ^{149}Ce, ^{100}Sr

TABLE I. The most probable fission channels for binary ($A_1 + A_2$) and ternary ($A_1 + A_2 + {}^4$He) fragment combination for ECT configuration of ^{252}Cf nucleus for optimum (compact and elongated) and without optimum [where $(\theta_1, \theta_2) = (90^\circ{-}90^\circ)$, $(0^\circ{-}0^\circ)$, $(0^\circ{-}90^\circ)$, and $(90^\circ{-}0^\circ)$] cases. The corresponding neutron (N), proton (Z) numbers and quadrupole deformations (β_{21}, β_{22}) of emitted fragments are presented below.

Cold-elongated/$0^\circ{-}0^\circ$		Hot-compact/$90^\circ{-}90^\circ$/$0^\circ{-}90^\circ$/$90^\circ{-}0^\circ$	
Binary	Ternary	Binary	Ternary
^{100}Zr + ^{152}Ce	^{92}**Kr** + ^{156}**Nd**	^{116}Pd + ^{136}Te	^{108}**Mo** + ^{140}**Xe**
(60,40 + 94,58)	(56,36 + 96,60)	(70,46 + 84,52)	(66,42 + 86,54)
(0.358,0.261)	(0.2280,0.279)	(−0.250,0.00)	(0.333,0.116)
^{101}Zr + ^{151}Ce	^{93}Kr + ^{155}Nd	^{117}Pd + ^{135}Te	^{109}Mo + ^{139}Xe
(61,40 + 93,58)	(57,36 + 95,60)	(71,46 + 83,52)	(67,42 + 85,54)
(0.368,0.252)	(0.265,0.279)	(−0.258,−0.008)	(0.334,0.100)
^{102}**Zr** + ^{150}**Ce**	^{94}Kr + ^{154}Nd	^{118}Pd + ^{134}Te	^{110}Mo + ^{138}Xe
(62,40 + 92,58)	(58,36 + 94,60)	(72,46 + 82,52)	(68,42 + 84,54)
(0.369,0.252)	(0.310,0.270)	(−0.240,0.00)	(0.335,0.00)
^{103}**Zr** + ^{149}**Ce**	^{95}Rb + ^{153}Pr	^{119}Ag + ^{133}Sb	^{111}Mo + ^{137}Xe
(63,40 + 91,58)	(58,37 + 94,59)	(72,47 + 82,51)	(69,42 + 83,54)
(0.380,0.235)	(0.329,0.270)	(−0.258, −0.008)	(0.336,−0.018)
^{104}**Zr** + ^{148}**Ce**	^{96}**Sr** + ^{152}**Ce**	^{120}Cd + ^{132}Sn / ^{120}Pd + ^{132}Te / ^{120}Pd + ^{132}Te / ^{120}Cd + ^{132}Sn	^{112}Ru + ^{136}Te / ^{112}Mo + ^{136}Xe / ^{112}Mo + ^{136}Xe / ^{112}Ru + ^{136}Te
(64,40 + 90,58)	(58,38 + 94,58)	(72,48 + 82,50)/(74,46 + 80,52)/(74,46 + 80,52)/(72,48 + 82,50)	(68,44 + 84,52)/(70,42 + 82,54)/(70,42 + 82,54)/(68,44 + 84,52)
(0.381,0.216)	(0.338,0.261)	(0.135,0.00)/(−0.188,0.00)/(−0.188,0.00)/(0.135,0.00)	(−0.258,0.00)/(0.337,0.00)/(0.337,0.00)/(−0.258,0.00)
^{105}Nb + ^{147}La	^{97}Sr + ^{151}Ce	^{121}Cd + ^{131}Sn / ^{121}Pd + ^{131}Te / ^{121}Pd + ^{131}Te / ^{121}Cd + ^{131}Sn	^{113}Ru + ^{135}Te / ^{113}Nb + ^{135}Cs / ^{113}Nb + ^{135}Cs / ^{113}Ru + ^{135}Te
(64,41 + 90,57)	(59,38 + 93,58)	(73,48 + 81,50)/(75,46 + 79,52)/(75,46 + 79,52)/(73,48 + 81,50)	(69,44 + 83,52)/(72,41 + 80,55)/(72,41 + 80,55)/(69,44 + 83,52)
(0.391,0.217)	(0.349,0.252)	(0.135,0.008)/(−0.162,0.00)/(−0.162,0.00)/(0.135,0.008)	(−0.258, −0.008)/(0.424,0.00)/(0.424,0.00)/−0.258, −0.008)
^{106}**Mo** + ^{146}**Ba**	^{98}**Sr** + ^{150}**Ce**	^{122}Cd + ^{130}Sn	^{114}Ru + ^{134}Te
(64,42 + 90,56)	(60,38 + 92,58)	(74,48 + 80,50)	(70,44 + 82,52)
(0.361,0.199)	(0.357,0.252)	(0.108,0.00)	(−0.258,0.00)
^{107}**Mo** + ^{145}**Ba**	^{99}Y + ^{149}La	^{123}Cd + ^{129}Sn / ^{123}Ag + ^{129}Sb / ^{123}Cd + ^{129}Sn / ^{123}Cd + ^{129}Sn	^{115}Rh + ^{133}Sb
(65,42 + 89,56)	(60,39 + 92,57)	(75,48 + 79,50)/(76,47 + 78,51)/(75,48 + 79,50)/(75,48 + 79,50)	(71,44 + 82,51)
(0.352,0.183)	(0.368,0.244)	(0.116,0.00)/(−0.258, −0.008)/(0.116,0.00)/(0.116,0.00)	(−0.258, −0.008)
^{108}**Mo** + ^{144}**Ba**	^{100}**Zr** + ^{148}**Ba**	^{124}Cd + ^{128}Sn	^{116}Pd + ^{132}Sn
(66,42 + 88,56)	(60,40 + 92,56)	(76,48 + 78,50)	(70,46 + 82,50)
(0.333,0.164)	(0.358,0.236)	(0.00,0.00)	(−0.250,0.00)

TABLE I. (*Continued.*)

Cold-elongated/$0^\circ-0^\circ$		Hot-compact/$90^\circ-90^\circ/0^\circ-90^\circ/90^\circ-0^\circ$	
Binary	Ternary	Binary	Ternary
^{109}Mo + ^{143}Ba	^{101}Y + ^{147}La	^{125}Cd + ^{127}Sn / ^{125}Cd + ^{127}Sn / ^{125}In + ^{127}In / ^{125}In + ^{127}In	^{117}Pd + ^{131}Sn
(67,42 + 87,56)	(62,39 + 90,57)	(77,48 + 77,50)/(77,48 + 77,50)/76,49 + 78,49)/(76,49 + 78,49)	(71,46 + 83,50)
(0.334,0.155)	(0.379,0.217)	(0.00,0.00)/(0.00,0.00)/(0.053,0.027)/(0.053,0.027)	(−0.258,0.008)
^{110}Mo + ^{142}Ba	^{102}**Zr** + ^{146}**Ba**	^{126}Cd + ^{126}Sn	^{118}Pd + ^{130}Sn
(68,42 + 86,56)	(62,40 + 90,56	(78,48 + 76,50)	(72,46 + 84,50)
(0.335,0.135)	(0.369,0.199)	(0.00,0.00)	(−0.240,0.000)
	^{103}**Zr** + ^{145}**Ba**		
	(63,40 + 89,56)		
	(0.380,0.183)		
	^{104}**Zr** + ^{144}**Ba**		
	64,40 + 88,56)		
	(0.381,0.164)		
	^{105}Nb + ^{143}Cs		
	(64,41 + 88,55)		
	(0.391,0.164)		
	^{106}**Mo** + ^{142}**Xe**		
	(64,42 + 88,54)		
	(0.361,0.145)		
	^{107}**Mo** + ^{141}**Xe**		
	(65,42 + 87,54)		
	(0.352,0.135)		
	^{108}**Mo** + ^{140}**Xe**		
	(66,42 + 86,54)		
	(0.333,0.116)		
	^{109}Mo + ^{139}Xe		
	(67,42 + 85,54)		
	(0.334,0.100)		
	^{110}Mo + ^{138}Xe		
	(68,42 + 84,54)		
	(0.335,0.00)		

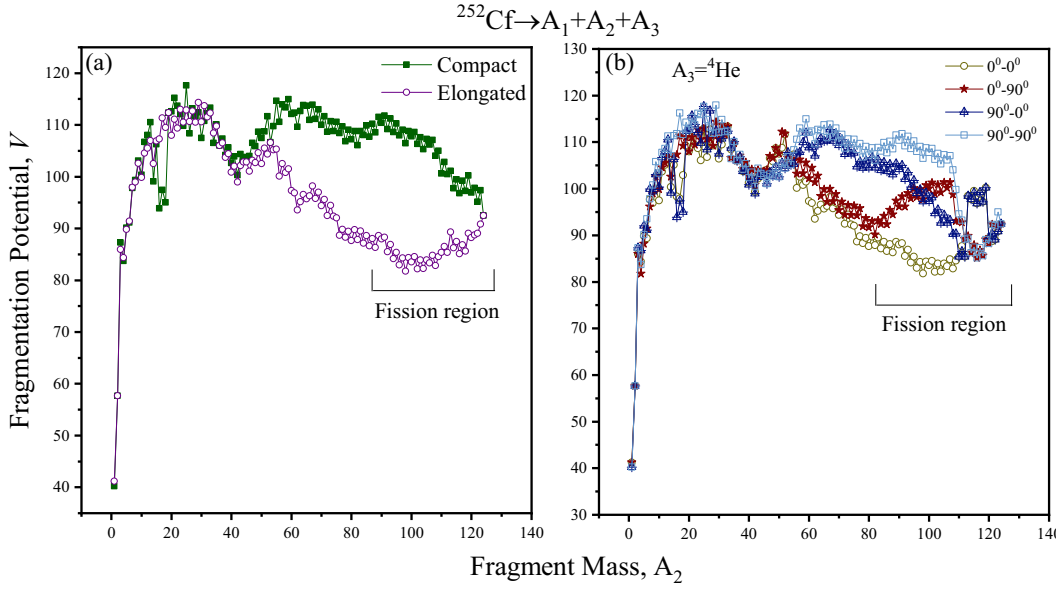

FIG. 3. Ternary fragmentation potential V(MeV) for ^{4}He-accompanied fission is plotted as a function of fragment mass number A_2 with the inclusion of quadrupole deformation corresponding to (a) with optimum orientation (hot-compact and cold-elongated) (b) with fixed orientation [where $(\theta_1, \theta_2) = (90^\circ - 90^\circ)$, $(0^\circ - 0^\circ)$, $(0^\circ - 90^\circ)$, and $(90^\circ - 0^\circ)$].

$(N_1 = 62,\ Z_1 = 38) + {}^{148}\text{Ce}, {}^{100}\text{Zr}$ $(N_1 = 60,\ Z_1 = 40) + {}^{148}\text{Ba}$, ${}^{102}\text{Zr}(N_1 = 62,\ Z_1 = 40) + {}^{146}\text{Ba}$, ${}^{103}\text{Zr}(N_1 = 63,\ Z_1 = 40) + {}^{145}\text{Ba}$, ${}^{104}\text{Zr}(N_1 = 64,\ Z_1 = 40) + {}^{144}\text{Ba}$, ${}^{106}\text{Mo}(N_1 = 64,\ Z_1 = 42) + {}^{142}\text{Xe}(N_1 = 65,\ Z_1 = 42)$, ${}^{107}\text{Mo}(N_1 = 65,\ Z_1 = 42) + {}^{141}\text{Xe}$, ${}^{108}\text{Mo}(N_1 = 66,\ Z_1 = 42) + {}^{140}\text{Xe}$, ${}^{116}\text{Pd} + {}^{132}\text{Sn}(N_1 = 82, Z_1 = 50)$ are experimentally detected [20,22]. The emergence of these fragments is related to the deformed neutron ($N = 60$ and 62) and proton ($Z = 38$) magicities, demonstrating alignment with experimental data. The majority of the identified fragments from ternary fission are prolate nuclei, further affirming the significant roles played by orientations and deformations in the analysis of decay phenomena. Henceforth, the present calculations show a reasonable agreement with experimental data as well as theoretical data. Many theoretical models [35,37,45] are employed to study ternary fragmentation processes by using different orientations and deformations. Our model shows a reasonable agreement with these theoretical studies where fragments like ${}^{116}\text{Pd} + {}^{132}\text{Sn}$ and ${}^{150}\text{Ce} + {}^{98}\text{Sr}$ are identified. Furthermore, to enhance the precision of fragment identification, we also intend to investigate charge minimization in the future.

B. Comparison between ECT and CCT configuration

In the preceding section, our focus was on comprehending the impact of deformations and orientations on the decay dynamics of the radioactive nucleus ^{252}Cf. The binary and ternary fragmentation potentials were worked out for different choices of orientation degrees of freedom. For ternary decay, we investigated the ECT configuration, with the third fragment being a light nucleus, such as an α particle. In this section, we have analyzed the influence of distinct configurations, namely ECT [shown in Fig. 4(a)] and CCT [shown in Fig. 4(b)] in the context of the ternary fission of ^{252}Cf with the inclusion of deformations and orientations. The ternary decay of ^{252}Cf involves the emission of various third fragments, such as hydrogen (H), helium (He), lithium (Li), boron (B), carbon (C), nitrogen (N), oxygen (O), fluorine (F), neon (Ne), sodium (Na), aluminum (Al), magnesium (Mg), and so on [2,14–20]. A multitude of theoretical models and experimental data have concluded that the ECT configuration is more appropriate when the emitted third fragment is relatively light. Conversely, when dealing with a heavier third fragment, the CCT configuration becomes more probable [36].

To understand these decay modes, $A_3 = {}^{30}\text{Mg}$ is considered as a fixed third fragment and the three-body fragmentation potential of ^{252}Cf nucleus is plotted in Figs. 5(a) and 5(b) for ECT and CCT configurations, respectively. This figure shows that the structure of the fission valley and magnitude are significantly modified when one moves from ECT to CCT. This may be due to the larger interaction radius of CCT mode as the third fragment is in between the other two heavier fragments. It leads to decrease in Coulomb potential between two heavier fragments. Hence, the fragmentation potential for CCT mode is less as compared to ECT mode. A closer look of Fig. 5 shows that hot-compact orientation gives the highest magnitude of fragmentation potential, whereas cold-elongated orientation gives lowest. This is because the interaction radius starts decreasing as one moves from elongated to compact orientations. Note that the fragmentation potential's deep valley gives the most probable fragments compared to neighboring fragments. Consequently, a dip in the fragmentation potential is observed for fragments with either magic proton/neutron numbers or near magic shell closure (spherical or deformed). From Fig. 5, one can see that for ECT configuration the most

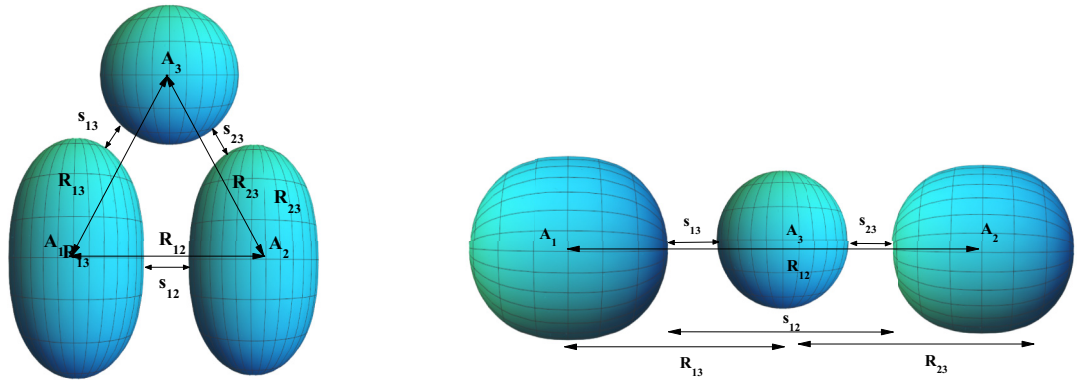

(a) Equatorial cluster tripartition (ECT)

(b) Collinear cluster tripartition (CCT)

FIG. 4. (a) ECT and (b) CCT configurations of two deformed heavy nuclei (A_1 and A_2) with the spherical third fragment. R_{ij} is the distance between the center of two nuclei and s_{ij} is the surface separation distance between the nuclei.

probable fission fragments for optimum orientation, i.e., compact (or spherical) [^{88}Se($Z = 34$, $N = 54$) + ^{134}Te($Z = 52$, N = **82**)+ ^{30}Mg($Z = 12$, $N = 18$)] and elongated [^{92}Kr($Z =$ **36**, $N = 56$)+ ^{130}Sn($Z =$ **50**, $N = 80$)+ ^{30}Mg($Z = 12$, $N = 18$)] are different. For the CCT configuration the most probable fragments remain the same, i.e., ^{92}Kr($Z = 36$, $N = 56$) + ^{130}Sn($Z =$ **50**, $N = 80$)+ ^{30}Mg($Z = 12$, $N = 18$) for the compact, spherical and elongated case. Further, the different sets of angles where orientations are set to fix (as studied earlier) are calculated and shown in Fig. 6 for ECT and CCT modes. From Figs. 6(a) and 6(b) one can observe that the fixed orientation choices significantly affect the fission valley's structure and magnitude for both configurations (ECT and CCT). The fragment combinations for ECT configuration with different fixed orientations are shown in Fig. 6(c), i.e., for $0°-0°/90°-0°$ it is ^{92}Kr($Z = 36$, $N = 56$) + ^{130}Sn($Z =$ **50**, $N = 80$) + ^{30}Mg($Z = 12$, $N = 18$) and for $0°-90°/90°-90°$ it is ^{88}Se($Z = 34$, $N = 54$) + ^{134}Te($Z = 52$, $N =$ **82**) + ^{30}Mg($Z = 12$, $N = 18$). Similarly, for different fixed orientations with CCT configuration, the fragments are shown in Fig. 6(d) for different angles is ^{90}Kr($Z =$ **36**, $N = 54$) + ^{132}Sn($Z =$ **50**, $N = 80$) + ^{30}Mg($Z = 12$, $N = 18$). The proton and neutron numbers are also mentioned along the fragment combination. The proton and neutron magic shell closure (spherical and deformed) of all the fragments are marked with bold letters. The fragments Kr and Sn with $A_3 = {}^{30}$Mg are identified as the most probable fragments. Although there is no experimental evidence of these fragments, our results show reasonable agreement with theoretical studies [34], as the identified fission fragments ^{88}Se + ^{134}Te are the same.

Several experimental studies have indicated the presence of calcium as a third fragment in the decay of ^{252}Cf [42,81]. To delve deeper into this phenomenon, additional calculations have been conducted, wherein the third fragment is taken to be $A_3 = {}^{48}$Ca. To gain a more comprehensive understanding of the underlying processes the fragmentaion potential is plotted for ECT and CCT cases. The calculations are done by considering spherical as well as deformed (hot-compact and cold-elongated) choice of nuclei. The magnitude and structure are significantly modified when one moves from the ECT to the CCT configuration but the most probable fission fragments remain the same, i.e., for compact (and spherical) the

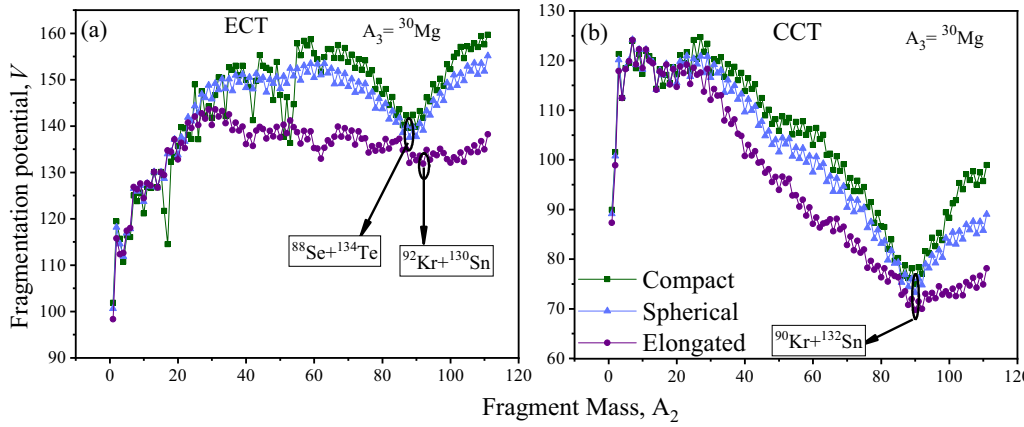

FIG. 5. Ternary fragmentation potential (V) is plotted with respect to A_2, for $A_3 = {}^{30}$Mg with (a) ECT and (b) CCT configuration with optimum orientations (compact, elongated, and spherical).

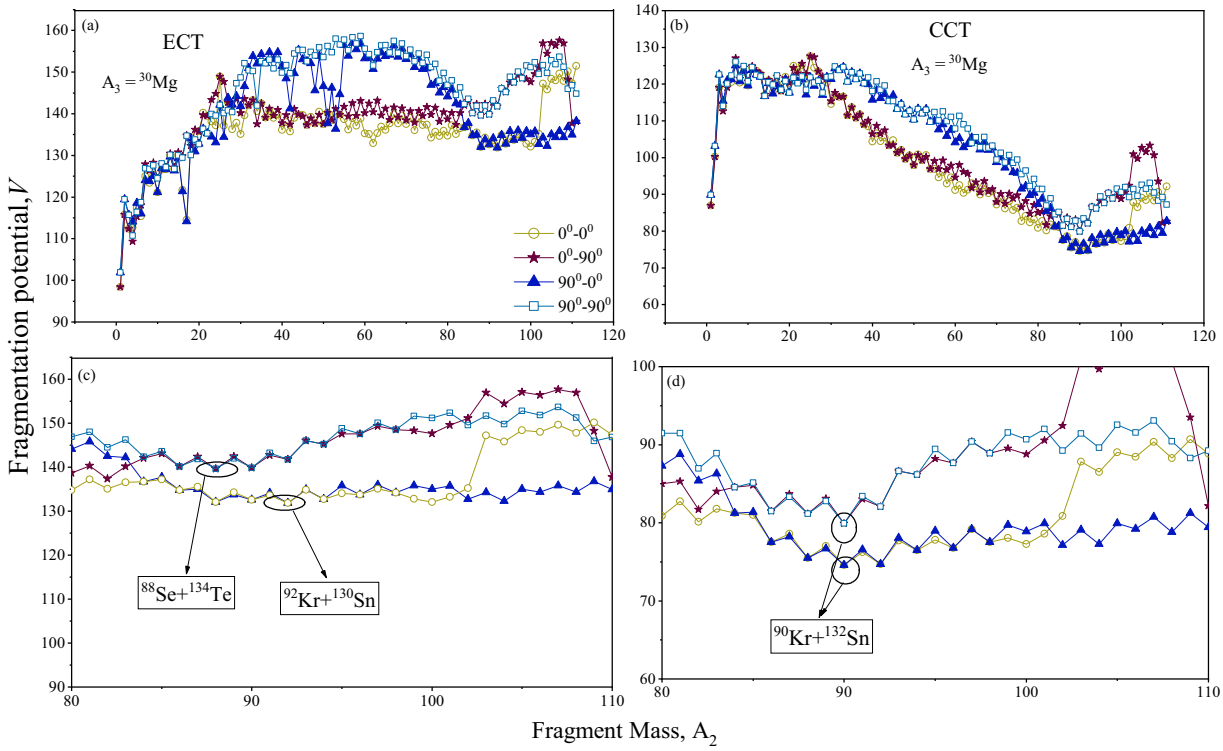

FIG. 6. Ternary fragmentation potential (V) is plotted with respect to A_2 for $A_3 = {}^{30}$Mg [(a) and (c)] using ECT and [(b) and (d)] CCT modes for $\theta_1, \theta_2 = (90°-90°), (0°-0°), (0°-90°), (90°-0°)$.

most probable fission fragment is ^{72}Ni($Z = \mathbf{28}$, $N = 44$) + ^{132}Sn($Z = \mathbf{50}, N = \mathbf{82}$) + ^{48}Ca($Z = \mathbf{20}, N = \mathbf{28}$), whereas for the cold-elongated (β_2-deformed) arrangement, fragments are ^{72}Ni($Z = \mathbf{28}, N = 44$) + ^{132}Sn($Z = \mathbf{50}, N = \mathbf{82}$) + ^{48}Ca($Z = \mathbf{20}, N = \mathbf{28}$) and ^{100}Sr($Z = \mathbf{38}, N = \mathbf{62}$)+ ^{104}Zr($Z = 40, N = 64$) + ^{48}Ca($Z = \mathbf{20}, N = \mathbf{28}$). From Fig. 7, one can observe that the deformations significantly change the magnitude as well as structure of the fragmentation potential for both configurations (ECT and CCT). This phenomenon arises from the fact that the interaction radius diminishes when

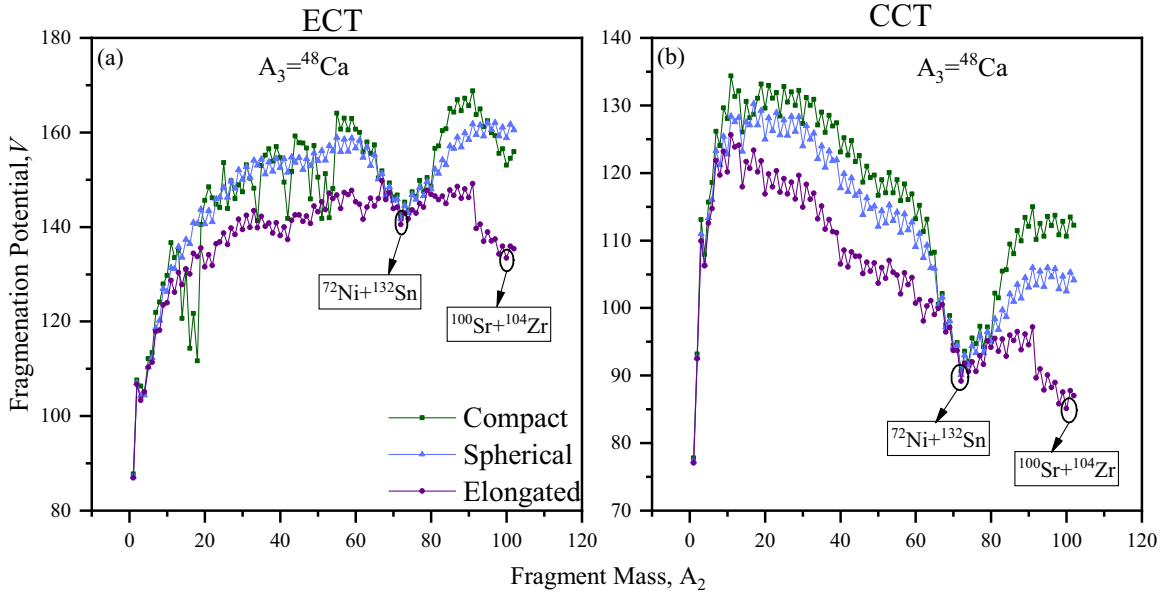

FIG. 7. Ternary fragmentation potential $V(A_2)$ calculated with $A_3 = {}^{48}$Ca for ^{252}Cf radioactive nucleus using (a) ECT and (b) CCT emmision modes.

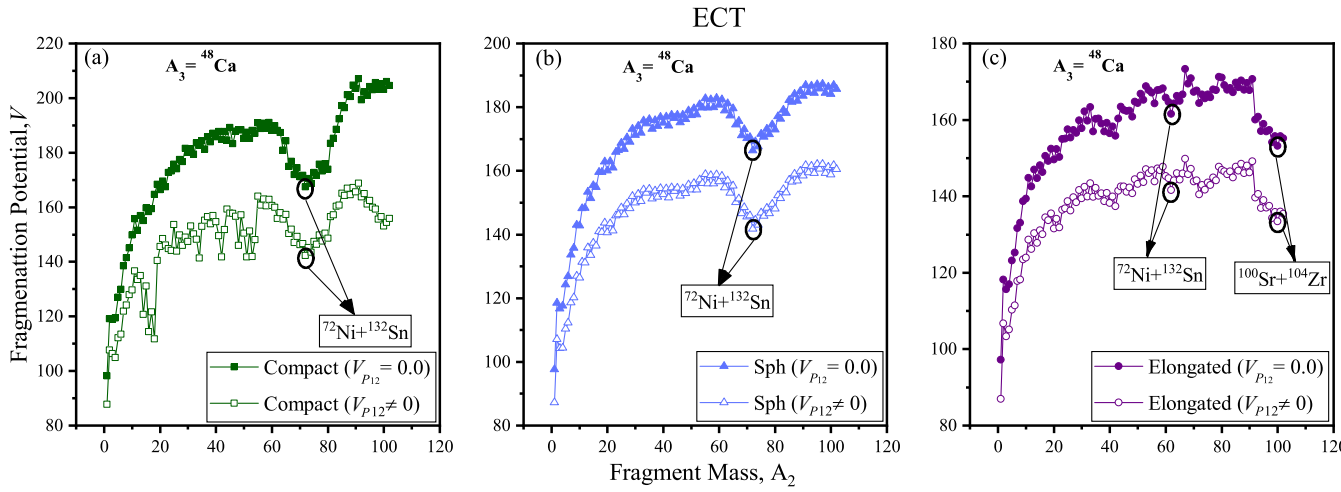

FIG. 8. Ternary fission fragmentation potential plotted with respect to A_2 for ^{252}Cf nucleus with $A_3 = {}^{48}$Ca, for ECT mode comparing (a) compact, (b) spherical, and (c) elongated by considering $V_{P_{12}}$ as zero and nonzero.

transitioning from a cold-elongated to a spherical (or hot-compact) configuration.

This, in turn, significantly impacts the fragmentation potential, given its strong dependence on deformations and interaction radius. Notably, a pronounced dip becomes evident in the context of fragments ^{72}Ni and ^{132}Sn, considering the third fragment $A_3 = {}^{48}$Ca, in both the spherical and deformed scenarios. This observation may be attributed to one of the fragments exhibiting shell closure and displaying no deformations. In contrast, another dip emerges in the fragmentation potential in the cold-elongated state, particularly in the case of the combination $^{100}\mathrm{Sr} + {}^{104}\mathrm{Zr}$. This could be attributed to substantial deformations, as these nuclei exhibit a prolate shape, and one of the fragments demonstrates a deformed magic number. A notable observation is that the favored fragments, driven by their lower fragmentation potential, remain consistent irrespective of the choice between the cluster tripartition configurations. Additionally, it is evident from the figures that the fission valley in the CCT case is more probable than that in the ECT case. This leads to the conclusion that the CCT configuration is more probable than the ECT configuration when considering the third fragment $A_3 = {}^{48}$Ca. This may be because the CCT has a larger interaction radius as the third fragment is heavy and lies in between the other two heavy fragments. CCT mode is studied by Pyatkov for ^{252}Cf nucleus [41–43] using the missing mass method. In these investigations, fission fragments such as Ni/Sn were detected through the utilization of the FOBOS setup at JINR. The third fragment was determined using the missing mass method. Consequently, the current calculations exhibit reasonable agreement with experimental data, with the most probable fragments being $^{132}\mathrm{Sn} + {}^{48}\mathrm{Ca} + {}^{72}\mathrm{Ni}$.

Based on the preceding analysis, it can be deduced that the CCT configuration is better suited for the heavier third fragment. The fragmentation potential, which comprises binding energy, nuclear potential, and Coulomb potential, plays a crucial role in understanding the behavior of the fragments. Among these, the nuclear proximity potential short-range, is particularly relevant for understanding the interactions between the fragments. To gain further insight into the proximity potential, we calculate the fragmentation potential with and without considering the proximity potential between two heavier fragments with different configurations, specifically the ECT and CCT configurations. The results are shown in Figs. 8 and 9. Here V_{P12} represents the proximity potential between two fragments (A_1 and A_2). It is evident from the representation that in the ECT configuration, the contribution of V_{P12} is significant, as indicated by the substantial difference for deformed as well as spherical cases. In contrast, for the CCT configuration, the influence of V_{P12} is negligible, with minimal difference between the potentials. This can be attributed to the substantial interfragment distance between A_1 and A_2, resulting in a reduction of potential within the CCT setup. This effect becomes particularly pronounced for heavier third fragments. In the specific scenario described here, the third fragment is taken as ^{48}Ca. Hence, one can conclude that the proximity potential plays more relatively salient role in the case of CCT configurations.

C. Ternary fragmentation yields

Further, based on theoretical [34,59,82–84] as well as experimental [20] investigations, the relative yield for the spontaneous ternary fission of ^{252}Cf is studied by taking various choices of the third fragment. Relative yield for the fission valley is calculated as the ratio of the penetration probability of a given fragment over the sum of penetration probabilities of all possible fragmentations as given in Eq. (14). In the present study, we calculate the yield by considering β_2 deformations with cold-elongated orientation, employing the ECT configuration [shown in Fig. 1(b)], taking $A_3 = {}^{4}$He for the spontaneous ternary fission of ^{252}Cf and is illustrated in Fig. 10. This can be easily understood as the nuclei in the region $92 \leqslant A_2 \leqslant 110$ exhibit predominantly prolate-deformed shapes. This dominance strongly influences the elongated yield as the interaction radius increases for these

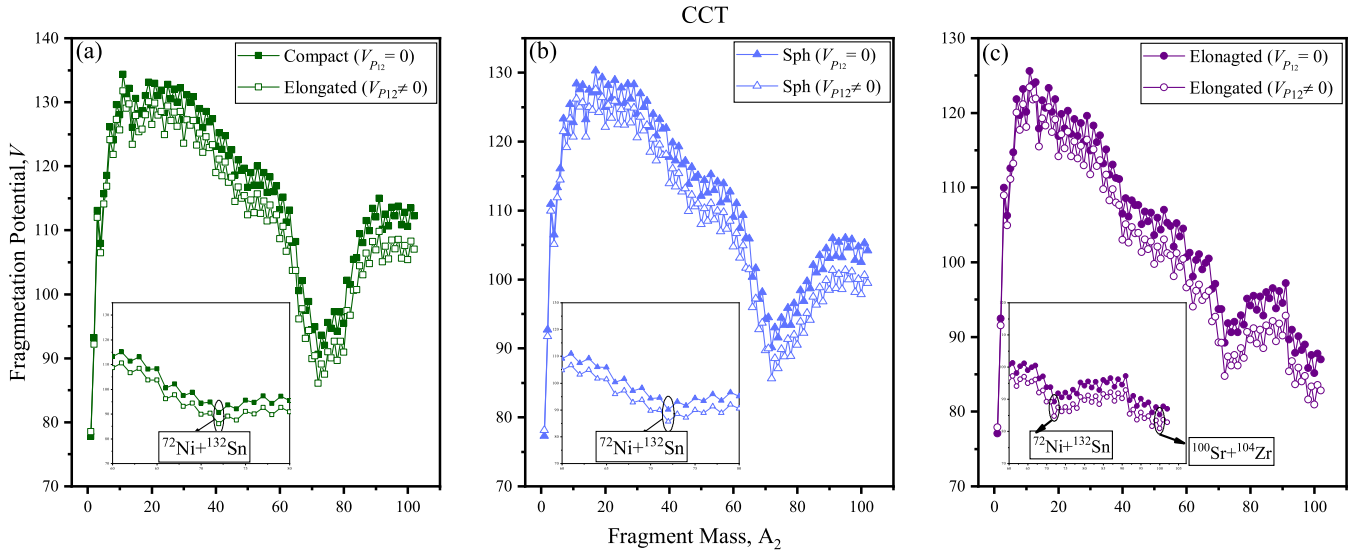

FIG. 9. Ternary fission fragmentation potential plotted with respect to A_2 for ^{252}Cf with $A_3 = {}^{48}$Ca for ECT mode comparing (a) compact, (b) spherical, and (c) elongated potentials by considering V_{P12} as zero and nonzero case.

fragments. The specific fragments identified in this context are highlighted and detailed in Table I. In Fig. 10, we also present the comparison of our calculated ternary yield for the ^{4}He spontaneous ternary fission of ^{252}Cf with available experimental data [20], and it shows a reasonable agreement with it. Furthermore, yield for $A_3 = {}^{30}$Mg and ^{48}Ca for two extreme orientations, i.e., elongated and compact and comparison is made with the spherical choice of fragments, as shown in Figs. 11 and 12. It is essential to highlight that lighter third fragments favor the ECT configuration. Consequently, for $A_3 = {}^4$He, ECT is utilized to compute the relative yield. However, for heavier third fragment both ECT and CCT configurations become significant. In order to understand both the processes, relative yield of ^{30}Mg is calculated using ECT and CCT is employed for relatively heavier third fragment ^{48}Ca. In Fig. 11, compact, elongated, and spherical orientations are presented by taking ECT configuration, revealing a preference for asymmetric distribution. For the elongated orientation, the most probable fragments are ^{92}Kr($Z = 36$, $N = 56$) + ^{130}Sn($Z = \mathbf{50}, N = 80$) + ^{30}Mg($Z = 12, N = 18$), while for the compact and spherical configuration the most probable fragments are ^{90}Kr($Z = 36$, $N = 54$) + ^{132}Sn($Z = \mathbf{50}, N = 80$) + ^{30}Mg($Z = 12, N = 18$). These findings exhibit reasonable agreement with theoretical data [34], particularly in observing asymmetric distribution in the tripartition of the ^{252}Cf nucleus with $A_3 = {}^{30}$Mg. Further, Fig. 12 illustrates the relative yield with $A_3 = {}^{48}$Ca, encompassing compact, elongated and spherical orientations by taking CCT configuration [as shown in Fig. 4(b)]. Significantly, asymmetric peaks dominate, while an additional symmetric peak emerges in the case of elongated orientations. For the asymmetric peak, the most probable fragments consist of ^{72}Ni($Z = 28$, $N = 44$) + ^{132}Sn($Z = \mathbf{50}$, $N = \mathbf{82}$) + ^{48}Ca($Z = 20$, $N = 28$). On the other hand, the most probable fragments for the symmetric peak include ^{100}Sr($Z = \mathbf{38}, N = \mathbf{62}$) + ^{104}Zr($Z = 40, N = 64$) + ^{48}Ca($Z = 20$, $N = 28$). Here the results are in reasonable agreement with experimental [41–43] data. Therefore, we can conclude that the calculated relative yield for elongated orientation for $A_3 = {}^4$He fragment show better agreement with experimental data (see Fig. 10). Therefore, it is expected that elongated orientation criteria should work for heavier third fragments, i.e., ^{30}Mg and ^{48}Ca. Further, the spherical and compact orientations are reported for comparative analysis and future reference/validations. This observation underscores the relevance of deformations and shell effects

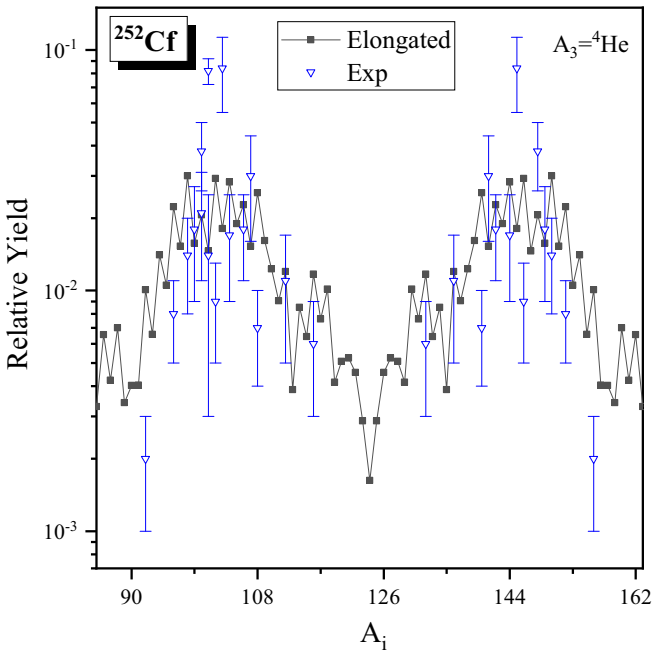

FIG. 10. The calculated relative yield for the ^{4}He accompanied ternary fission of ^{252}Cf is compared with experimental data.

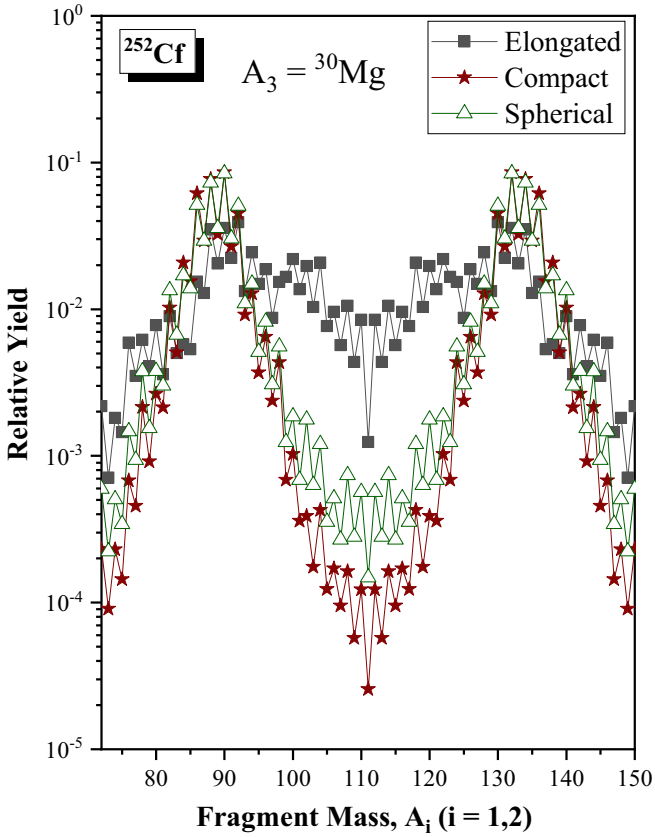

FIG. 11. The calculated relative yield for ternary fission of ^{252}Cf by taking $A_3 = {}^{30}$Mg considering ECT configuration is plotted as a function of fragment mass numbers A_1 and A_2. Comparing elongated, compact and spherical orientations.

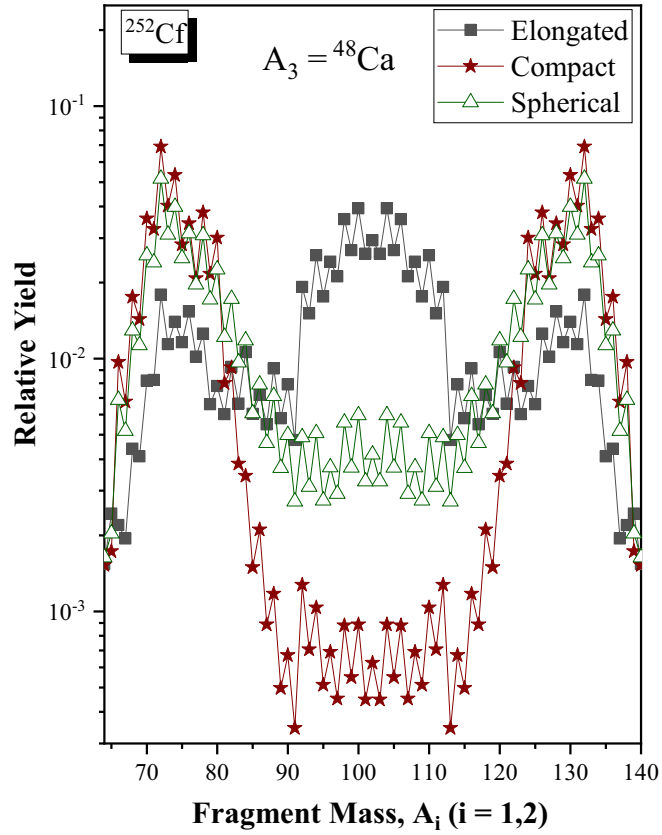

FIG. 12. The calculated relative yield for the ^{48}Ca accompanied ternary fission of ^{252}Cf nucleus using elongated, spherical and compact orientations by considering CCT configuration.

in identifying ternary fission fragments in view of different orientation criteria.

IV. SUMMARY

The spontaneous binary and ternary fission of ^{252}Cf is studied within PCM and TCM, respectively. For both (binary and ternary decay), the fragmentation potential is computed by including β_2 deformations with in possible orientation. For both the decay modes, the fission fragment mass distribution changes from symmetric to asymmetric as one moves from optimum hot-compact configuration to optimum cold-elongated. This is due to the fact that the interaction radius decreases as one goes from cold-elongated optimum to compact-optimum configuration. The β_2 deformed hot-compact/$90^\circ-90^\circ/0^\circ-90^\circ/90^\circ-0^\circ$ configuration shows the dominance of symmetric and near-symmetric decay channels with prominent influence of spherical magic shell closure. However, the cold-elongated/$0^\circ-0^\circ$ orientation (β_2 deformed) approach shows asymmetric distribution with the dominance of deformed magic shell closure.

It is observed that the magnitude and structure of fragmentation potential is significantly modified when one shifts from the ECT to the CCT configuration. Moving from the case of intermediate ($A_3 = {}^{30}$Mg) to heavier ($A_3 = {}^{48}$Ca) third fragment, the CCT mode starts competing with the ECT one. The heavier third fragment shows a prominent dip in CCT mode as the interfragment distance is large and results in a lower magnitude of proximity and Coulomb potential. This dip corresponds to ^{72}Ni($Z = \mathbf{28}$, $N = 44$) + ^{132}Sn($Z = \mathbf{50}$, $N = \mathbf{82}$)+ ^{48}Ca($Z = \mathbf{20}$, $N = \mathbf{28}$). Whereas, additional dip at ^{100}Sr($Z = \mathbf{38}$, $N = \mathbf{62}$)+ ^{104}Zr($Z = 40$, $N = 64$)+ ^{48}Ca($Z = \mathbf{20}$, $N = \mathbf{28}$) is observed for elongated configuration. Our calculations show that, one of the decaying fragments is associated with neutron/proton shell closure, which is consistent with experimental observations [41–43]. In addition to this, relative yield of different tripartition combinations is studied and compared with experimental data. The results obtained are aligned with the studies done so far. It is concluded that the deformations and orientations play a significant role in identifying the binary and ternary fission fragments. Hence, various orientation prospects are explored which may impart useful insights for future understanding of reaction dynamics on theoretical as well as experimental front. It will be of further interest to include higher-order deformation effects in such comparative analysis of binary and ternary fragmenataion.

ACKNOWLEDGMENT

Financial support from the Department of Science and Technology (DST), Science and Engineering Research Board (SERB) New Delhi, India in the form of a research project grant (File No. CRG/2021/001144) is gratefully acknowledged.

[1] G. M. Ter-Akopian, J. H. Hamilton, Y. T. Oganessian, J. Kormicki, G. S. Popeko, A. V. Daniel, A. V. Ramayya *et al.*, Phys. Rev. Lett. **73**, 1477 (1994).
[2] J. H. Hamilton, A. V. Ramayya *et al.*, J. Phys. G: Nucl. Part. Phys. **20**, L85 (1994).
[3] G. M. Ter-Akopian, J. H. Hamilton, Y. T. Oganessian *et al.*, Phys. Rev. C **55**, 1146 (1997).
[4] A. Sandulescu, A. Florescu, F. Carstoiu, W. Greiner, J. H. Hamilton, A. V. Ramayya, and B. R. S. Babu, Phys. Rev. C **54**, 258 (1996).
[5] S. L. Whetstone and T. D. Thomas, Phys. Rev. **154**, 1174 (1967).
[6] G. M. Raisbeck and T. D. Thomas, Phys. Rev. **172**, 1272 (1968).
[7] J. K. Hwang, A. V. Ramayya, J. H. Hamilton, C. J. Beyer *et al.*, Phys. Rev. C **61**, 047601 (2000).
[8] G. M. Ter-Akopian *et al.*, Phys. At. Nucl. **67**, 1860 (2004).
[9] G. K. Mehta, J. Poitou, M. Ribrag, and C. Signarbieux, Phys. Rev. C **7**, 373 (1973).
[10] Z. Fraenkel, Phys. Rev. **156**, 1283 (1967).
[11] A. Sandulescu, S. Misicu, F. Carstoiu, and W. Greiner, Phys. Part. Nuclei **30**, 386 (1999).
[12] M. L. Muga, H. R. Bowman *et al.*, Phys. Rev. **121**, 270 (1961).
[13] D. Poenaru, W. Greiner, J. Hamilton, and A. Ramayya, J. Phys. G: Nucl. Part. Phys. **27**, L19 (2001).
[14] K. Manimaran and M. Balasubramaniam, Phys. Rev. C **79**, 024610 (2009).
[15] N. Sharma, A. Kaur, and M. K. Sharma, Phys. Rev. C **105**, 044602 (2022).
[16] A. V. Daniel, G. M. Ter-Akopian, J. H. Hamilton, A. V. Ramayya, J. Kormicki, G. S. Popeko, A. S. Fomichev, A. M. Rodin, Y. T. Oganessian, J. D. Cole, J. K. Hwang, Y. X. Luo, D. Fong, P. Gore, M. Jandel, J. Kliman, L. Krupa, J. O. Rasmussen, S. C. Wu, I. Y. Lee, M. A. Stoyer, R. Donangelo, and W. Greiner, Phys. Rev. C **69**, 041305(R) (2004).
[17] Y. N. Kopatch, M. Mutterer, D. Schwalm, P. Thirolf, and F. Gönnenwein, Phys. Rev. C **65**, 044614 (2002).
[18] A. Florescu, A. Sandulescu, D. S. Delion, J. H. Hamilton, A. V. Ramayya, and W. Greiner, Phys. Rev. C **61**, 051602(R) (2000).
[19] A. V. Ramayya, J. K. Hwang, J. H. Hamilton (GANDS95 Collaboration) *et al.*, Phys. Rev. Lett. **81**, 947 (1998).
[20] A. V. Ramayya, J. H. Hamilton *et al.*, Phys. Rev. C **57**, 2370 (1998).
[21] C. T. Goodin, D. Fong, J. K. Hwang, A. V. Ramayya, J. H. Hamilton, K. Li, Y. X. Luo, J. O. Rasmussen, S. C. Wu, M. A. Stoyer, T. N. Ginter, S. J. Zhu, R. Donangelo, G. M. Ter-Akopian, A. V. Daniel, G. S. Popeko, A. M. Rodin, and A. S. Fomichev, Phys. Rev. C **74**, 017309 (2006).
[22] A. Ramayya *et al.*, Prog. Part. Nucl. Phys. **46**, 221 (2001).
[23] L. Rosen and A. M. Hudson, Phys. Rev. **78**, 533 (1950).
[24] R. L. Fleischer, P. B. Price, R. M. Walker, and E. L. Hubbard, Phys. Rev. **143**, 943 (1966).
[25] R. H. Iyer and J. W. Cobble, Phys. Rev. **172**, 1186 (1968).
[26] V. Perelygin, N. Shadieva, S. Tretiakova, A. Boos, and R. Brandt, Nucl. Phys. A **127**, 577 (1969).
[27] H. Becker, P. Vater, R. Brandt, A. Boos, and H. Diehl, Phys. Lett. B **50**, 445 (1974).
[28] U. Köster, H. Faust, G. Fioni, T. Friedrichs, M. Groß, and S. Oberstedt, Nucl. Phys. A **652**, 371 (1999).
[29] C.-M. Herbach, D. Hilscher, V. Tishchenko *et al.*, Nucl. Phys. A **712**, 207 (2002).
[30] I. Tsekhanovich, Z. Büyükmumcu, M. Davi, H. O. Denschlag, F. Gonnenwein, and S. F. Boulyga, Phys. Rev. C **67**, 034610(R) (2003).
[31] F. Gnnenwein, Nucl. Phys. A **734**, 213 (2004).
[32] D. Poenaru, Y. Nagame, R. Gherghescu, W. Greiner, J. Hamilton, A. Ramayya *et al.*, Roman. Rep. Phys. **55**, 781 (2003).
[33] K. R. Vijayaraghavan, M. Balasubramaniam, and W. von Oertzen, Phys. Rev. C **91**, 044616 (2015).
[34] K. Manimaran and M. Balasubramaniam, Eur. Phys. J. A **45**, 293 (2010).
[35] K. Manimaran and M. Balasubramaniam, J. Phys. G: Nucl. Part. Phys. **37**, 045104 (2010).
[36] K. Manimaran and M. Balasubramaniam, Phys. Rev. C **83**, 034609 (2011).
[37] K. Santhosh and S. Krishnan, Eur. Phys. J. A **52**, 108 (2016).
[38] K. Santhosh, S. Krishnan, and B. Priyanka, J. Phys. G: Nucl. Part. Phys. **41**, 105108 (2014).
[39] W. M. Seif and A. S. Hashem, Phys. Rev. C **104**, 014616 (2021).
[40] W. von Oertzen and A. K. Nasirov, Eur. Phys. J. A **56**, 299 (2020).
[41] Y. V. Pyatkov, D. V. Kamanin, W. v. Oertzen *et al.*, Eur. Phys. J. A **45**, 29 (2010).
[42] Y. V. Pyatkov, D. V. Kamanin, W. v. Oertzen *et al.*, Eur. Phys. J. A **48**, 94 (2012).
[43] Y. V. Pyatkov, D. V. Kamanin, A. A. Alexandrov, I. A. Alexandrova *et al.*, Phys. Rev. C **96**, 064606 (2017).
[44] R. K. Gupta, W. Scheid, and W. Greiner, Phys. Rev. Lett. **35**, 353 (1975).
[45] K. R. Vijayaraghavan, M. Balasubramaniam, and W. von Oertzen, Phys. Rev. C **90**, 024601 (2014).
[46] W. von Oertzen, A. Nasirov, and R. Tashkhodjaev, Phys. Lett. B **746**, 223 (2015).
[47] R. B. Tashkhodjaev, A. K. Nasirov, S. A. Kalandarov, and O. K. Ganiev, Phys. Rev. C **107**, 044611 (2023).
[48] K. R. Vijayaraghavan, V. G. Lakshmi, P. Prema, and M. Balasubramaniam, J. Phys. G: Nucl. Part. Phys. **46**, 025103 (2019).
[49] R. K. Gupta, S. Singh, R. K. Puri, and W. Scheid, Phys. Rev. C **47**, 561 (1993).
[50] A. Sandulescu, A. Florescu, and W. Greiner, J. Phys. G: Nucl. Part. Phys. **15**, 1815 (1989).
[51] F. Gönnenwein and B. Börsig, Nucl. Phys. A **530**, 27 (1991).
[52] A. Florescu, A. Sandulescu *et al.*, J. Phys. G: Nucl. Part. Phys. **19**, 669 (1993).

[53] G. Sawhney, R. Kumar, and M. K. Sharma, Phys. Rev. C **86**, 034613 (2012).
[54] M. Kaur, M. K. Sharma, and R. K. Gupta, Phys. Rev. C **86**, 064610 (2012).
[55] R. K. Gupta, N. Singh, and M. Manhas, Phys. Rev. C **70**, 034608 (2004).
[56] M. Manhas and R. K. Gupta, Phys. Rev. C **72**, 024606 (2005).
[57] R. K. Gupta, M. Balasubramaniam *et al.*, J. Phys. G: Nucl. Part. Phys. **31**, 631 (2005).
[58] R. K. Gupta, Niyti, M. Manhas *et al.*, Int. J. Mod. Phys. E **18**, 601 (2009).
[59] C. Karthikraj and Z. Ren, Phys. Rev. C **101**, 014603 (2020).
[60] K. Sharma *et al.*, Eur. Phys. J. A **55**, 30 (2019).
[61] M. Ismail, W. Seif *et al.*, Ann. Phys. **372**, 375 (2016).
[62] M. Ismail, W. Seif, and A. Hashem, Eur. Phys. J. A **52**, 317 (2016).
[63] W. von Oertzen, B. Gebauer *et al.*, Eur. Phys. J. A **36**, 279 (2008).
[64] V. Denisov, Eur. Phys. J. A **58**, 188 (2022).
[65] H. Fink, J. Maruhn *et al.*, Zeitschr. Phys. **268**, 321 (1974).
[66] K. Sharma, G. Sawhney, M. K. Sharma, and R. K. Gupta, Nucl. Phys. A **972**, 1 (2018).
[67] A. Kaur, N. Sharma, and M. K. Sharma, Phys. Rev. C **103**, 034618 (2021).
[68] N. Sharma and M. K. Sharma, Phys. Rev. C **106**, 034608 (2022).
[69] J. Maruhn and W. Greiner, Phys. Rev. Lett. **32**, 548 (1974).
[70] G. Audi and A. Wapstra, Nucl. Phys. A **595**, 409 (1995).
[71] P. Moller, J. Nix, W. Myers, and W. Swiatecki, At. Data Nucl. Data Tables **59**, 185 (1995).
[72] C. Y. Wong, Phys. Rev. Lett. **31**, 766 (1973).
[73] N. Sharma, A. Kaur, and M. K. Sharma, Phys. Rev. C **102**, 064603 (2020).
[74] N. Malhotra and R. K. Gupta, Phys. Rev. C **31**, 1179 (1985).
[75] J. Błocki, J. Randrup, W. Swiatecki, and C. Tsang, Ann. Phys. **105**, 427 (1977).
[76] A. J. Baltz and B. F. Bayman, Phys. Rev. C **26**, 1969 (1982).
[77] G. Kaur, N. Grover, K. Sandhu, and M. K. Sharma, Nucl. Phys. A **927**, 232 (2014).
[78] S. Singh, S. Mahapatro, and R. Mishra, Int. J. Mod. Phys. E **22**, 1350018 (2013).
[79] P. Arumugam, B. K. Sharma, S. K. Patra, and R. K. Gupta, Phys. Rev. C **71**, 064308 (2005).
[80] B.-N. Lu, E.-G. Zhao, and S.-G. Zhou, Phys. Rev. C **84**, 014328 (2011).
[81] W. Von Oertzen, Y. Pyatkov, and D. Kamanin, Acta Phys. Pol. B **44**, 447 (2013).
[82] V. Y. Denisov, N. A. Pilipenko, and I. Y. Sedykh, Phys. Rev. C **95**, 014605 (2017).
[83] C. Karthikraj and Z. Ren, Phys. Rev. C **102**, 024607 (2020).
[84] J. B. Natowitz, H. Pais, and G. Röpke, Phys. Rev. C **107**, 014618 (2023).